Chemical Science

ROYAL SOCIETY OF CHEMISTRY

EDGE ARTICLE

View Article Online
View Journal | View Issue

Cite this: *Chem. Sci.*, 2025, **16**, 12994

All publication charges for this article have been paid for by the Royal Society of Chemistry

Received 28th March 2025
Accepted 30th May 2025

DOI: 10.1039/d5sc02354h

rsc.li/chemical-science

Nanoarchitectonics of cobalt/nitrogen-doped carbon with an unbalanced double primitive bicontinuous motif for efficient electrocatalysis†

Bin Zhao,[a] Bohan Liu,[a] Ji Han,[a] Ruigang Sun,[a] Haidong Xu,[a] Yuanbo Sun,[ab] Guangrui Chen,[ac] Zhaohui Shi,[a] Chenxu Liu,[a] Yanjing Gao,[a] Mingjie Zhang,[a] Song Lin Zhang,[d] Yusuke Yamauchi[efg] and Buyuan Guan *[ac]

In virtue of the smooth mass transfer and unique physical properties enabled by the special three-dimensional (3D) interconnected network, bicontinuous porous functional materials have received extensive attention in catalysis, energy conversion, and cargo delivery. However, endowing materials with meticulous inner bicontinuous geometries and achieving precise control over the pore structures remain a huge challenge. Herein, we report a facile heterogeneous interface-induced topological phase transition method to obtain unbalanced double primitive architectural cobalt/nitrogen-doped (Co/N-doped) carbon particles. The rationally designed dual metal–organic framework (MOF)-derived composite particles retain the original 3D channel with a single primitive cubic structure inherited from their precursors after the pyrolysis process. Noteworthily, a new set of continuous channels with the same topological structure is introduced into the originally solid pore wall by utilizing local thermal stability differences at the heterogeneous interface of two isostructural MOFs. The two sets of channels possess different volumes, presenting an unbalanced bicontinuous structure similar to $Im\bar{3}m$, with the Co–N_x active sites anchored on the derived thin pore walls. Benefiting from the high-efficiency mass transfer enabled by the 3D open channels of the bicontinuous structure and high surface utilization enabled by the local thin-wall nanotube structure, unbalanced bicontinuous structural Co/N-doped carbon catalysts exhibit enhanced electrocatalytic activity in the oxygen reduction reaction (ORR). The assembled Zn–air battery delivers high peak power density (215 mW cm^{-2}) and large specific capacity (766 mA h g^{-1}). This methodology provides new insights for universally constructing extra channels to achieve 3D periodic interpenetrating networks from the rational structural design and processing of porous materials with appropriate heterogeneous interfaces.

Introduction

Due to the adjustable electronic structure, high atomic utilization efficiency, and low cost, transition metal and nitrogen-doped carbon (M–N_x/C) catalysts have gained broad attention in the field of energy storage and conversion.[1–6] In virtue of their tunable compositions and adjustable pore structures, metal–organic frameworks (MOFs) can serve as ideal templates/precursors for the preparation of M–N_x/C with uniformly dispersed active sites.[7,8] Nevertheless, high-temperature treatment inevitably leads to the shrinkage or collapse of the original pore structure of MOFs, which significantly reduces the mass transfer efficiency of the reactants and mass-specific activity of the catalysts.[9] One feasible approach to address the diffusion limitation and increase the exposure ratio of the catalyst's active sites is to introduce open architectures into suitable catalysts.[10–12] Up to now, researchers have designed and constructed a series of highly open pore structures and nanostructures, achieving enhanced mass transfer efficiency,

[a]State Key Laboratory of Inorganic Synthesis and Preparative Chemistry, College of Chemistry, Jilin University, Qianjin Street 2699, Changchun 130012, P. R. China. E-mail: guanbuyuan@jlu.edu.cn

[b]Key Lab of Groundwater Resources and Environment, Ministry of Education, Jilin University, Changchun 130021, P. R. China

[c]International Center of Future Science, Jilin University, Qianjin Street 2699, Changchun 130012, P. R. China

[d]Institute of Materials Research and Engineering (IMRE), Agency for Science, Technology and Research (A*STAR), 2 Fusionopolis Way, Singapore 138634, Singapore

[e]School of Chemical Engineering and Australian Institute for Bioengineering and Nanotechnology (AIBN), The University of Queenslan, Brisbane QLD 4072, Australia

[f]Department of Materials Process Engineering, Graduate School of Engineering, Nagoya University, Furo-cho, Chikusa-ku, Nagoya, Aichi, 464-8603, Japan

[g]Department of Chemical and Biomolecular Engineering, Yonsei University, 50 Yonseiro, Seodaemun-gu, Seoul 03722, Republic of Korea

† Electronic supplementary information (ESI) available. See DOI: https://doi.org/10.1039/d5sc02354h

exposed surface area, and utilization of active sites by introducing secondary meso-/macropores and/or building low-dimensional nanostructures in active materials.[13–16] Therefore, the introduction of well-engineered open structures into M–N_x/C materials is expected to significantly alleviate the diffusion limitations and enhance their electrocatalytic performances for energy storage and conversion.

Among many unique pore structures, ordered bicontinuous structures can not only effectively enhance mass transfer and improve the utilization of active sites, but also endow materials with additional exceptional physical properties (*e.g.*, negative refraction and multiple equivalent magnetization configurations) due to their two sets of three-dimensional (3D) interpenetrating open networks and highly symmetrical structure.[17–22] Currently, constructing ordered bicontinuous structures primarily relies on evaporation-induced self-assembly or nanocasting to obtain inverse structures of the appropriate hard templates.[18] However, due to thermodynamic preferences, these methods typically result in two identical and highly symmetrical pore structures. This makes it challenging to modify the bicontinuous structures to form desirable deformed architectures, such as shifted structures by a constant distance off the normal double networks or unbalanced structures with unequal labyrinth volumes.[17,23–25] Meanwhile, evaporation-induced self-assembly and nanocasting using common silica-based hard templates involve relatively complex reaction systems and stringent template removal conditions,[26,27] which to some extent limits the variety of obtainable materials. Additionally, the materials obtained through the above methods often exhibit bulk forms with poor dispersion and restricted mass transfer due to relatively long pore channels, which limits their application in scenarios requiring high-efficiency utilization of the active area. Recent research indicates that bicontinuous microscale templates formed by the self-assembly of easily removable block copolymers can generally be used to synthesize well-dispersed spheres of various functional materials under mild conditions, especially including MOFs that can serve as ideal precursors for M–N_x/C.[28–30] Unfortunately, owing to the fact that such templates possess a set of sealed pores that framework precursors cannot enter, the resultant MOF materials can only use one set of channels to form the corresponding single-network architecture, and their derived M–N_x/C will inherit the thick pore walls in the MOF precursors, creating inaccessible dead volumes, which restrict the utilization efficiency of the overall materials. Therefore, it remains a significant challenge to circumvent the inherent limitations of traditional methods and introduce two sets of separately controllable pore channels into the M–N_x/C functional materials, enabling the formation of well-dispersed deformed bicontinuous micro-/nanostructures with thin pore walls that could enhance mass transfer, anchor more active sites at the reaction interface, and increase the utilization efficiency of the overall architectures.

Herein, we demonstrate a facile heterogeneous interface-induced topological phase transition method to obtain cobalt/nitrogen-doped carbon unbalanced double primitive bicontinuous particles (designated as Co/NC UDPPs). The double primitive (DP, $Im\bar{3}m$) structural templates are obtained by self-assembly of the block copolymer in a specific solvent system, and the ZIF-8 single primitive ($Pm\bar{3}m$) structural particles (denoted as ZIF-8 SPPs) are synthesized by *in situ* growth in one set of open channels of the polymer templates. Using ZIF-8 SPPs as the seed, ZIF-67 thin layers are epitaxially grown on the surface of ZIF-8 by lattice parameter matching to form the core–shell heterostructured ZIF-8@ZIF-67 SPPs. Finally, Co/NC UDPPs are formed by pyrolysis. The channels of Co/NC UDPPs, which are open to the external environment, inherit the 3D interconnected single primitive topological structure in their ZIF-8@ZIF-67 SPP precursors. During the process of thermal treatment, the *in situ* formed Co on the heterogeneous interface of the pore wall from the ZIF-67 side pulls the inner ZIF-8 matrix towards itself, forming a set of entirely new and relatively narrow $Pm\bar{3}m$ cubic structural continuous channels within the originally solid pore walls. The newly formed channels, along with the existing ones, exhibit an unbalanced (unequal volumes of pore space) triply periodic minimal surface structure similar to $Im\bar{3}m$ in space. These channels are interconnected through partially fractured thin graphitized pore walls. The unique pore structure not only enhances mass transfer, but also further promotes the exposure and utilization of Co–N_x active sites at the three-phase boundary (catalyst-electrolyte-oxygen). Thanks to the overall structural advantages, the catalyst exhibits outstanding catalytic performance in the oxygen reduction reaction (ORR). Furthermore, the Zn–air battery (ZAB) assembled with Co/NC UDPPs as the air cathode electrocatalyst demonstrates a peak power density of 215 mW cm^{-2} and a specific capacity of 766 mA h g^{-1}, surpassing those of the ZAB assembled with a Pt/C catalyst. This method provides a novel approach for rationally constructing unique deformed ordered bicontinuous architectures through delicately designing and possessing single network structures with heterogeneous interfaces, which are expected to exhibit enhanced performances in various application scenarios.

Results and discussion

The synthesis process of the sample is depicted in Fig. 1 and can be divided into four major steps. First, polymer cubosomes (PCs) with bicontinuous pore structures are synthesized according to the method reported in previous literature.[31] Synthesis of *block* copolymer polystyrene–poly(ethylene oxide) (PS-*b*-PEO) with a narrow molecular weight distribution is achieved *via* atom transfer radical polymerization (Fig. S1†). Afterwards, PCs with a DP cubic network are obtained by slowly dropping water into a dioxane (Diox)/*N*,*N*-dimethylformamide (DMF) mixed solution containing the PS-*b*-PEO. As shown in Fig. S2,† scanning electron microscopy (SEM) images of the PCs exhibit a near-spherical morphology, with an average diameter of 2.8 μm. Furthermore, mesopores with the size of ~25 nm are tetragonally distributed on the surface of the PCs. Transmission electron microscopy (TEM) images show bicontinuous pore channels inside the PCs, with an $Im\bar{3}m$ structure. The small-angle X-ray scattering (SAXS) pattern of PCs displays three

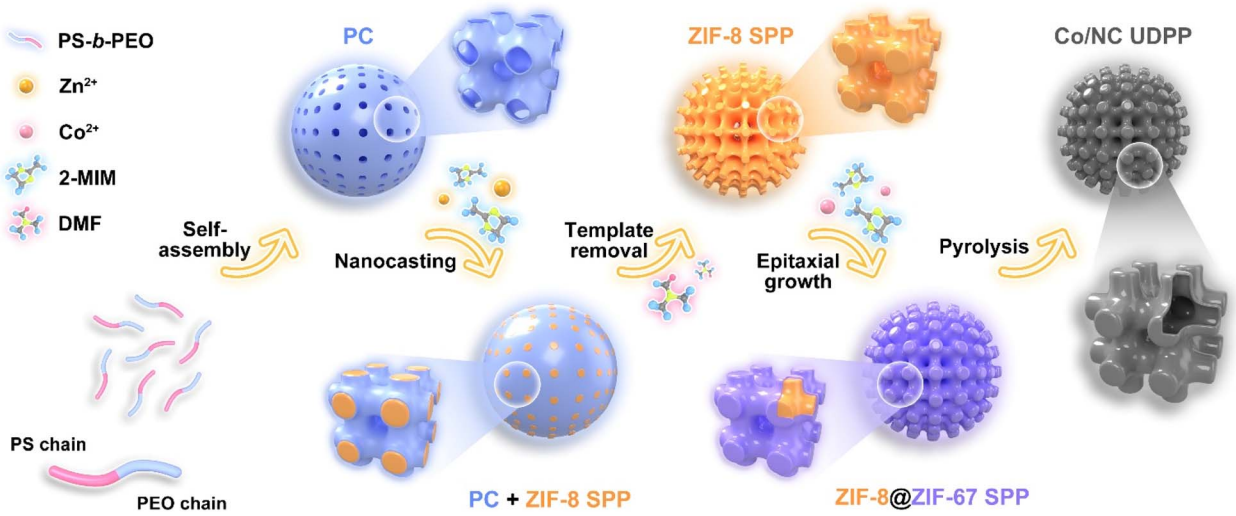

Fig. 1 Schematic illustration of the synthesis process of Co/NC UDPP.

characteristic peaks with a q ratio of $\sqrt{2}:\sqrt{4}:\sqrt{6}$, corresponding to the $Im\bar{3}m$ cubic structure's (110), (200), and (211) reflections (Fig. S3†). And then, 2-methylimidazole (2-MIM) is adsorbed into one set of open mesochannels of the PCs through capillary force and intermolecular interactions with PEO chains. Subsequent *in situ* coordination with added Zn^{2+} ions resulted in the formation of ZIF-8. The PC templates are then etched in DMF, yielding ZIF-8 with SP structure. SEM analysis reveals that ZIF-8 SPPs exhibit an average diameter consistent with that of the PC templates and display a well-ordered porous structure on their surfaces (Fig. S4a and b†). The measured pore diameter of ZIF-8 SPPs is approximately 50 nm. The TEM images and SAXS pattern further confirm ZIF-8 SPPs possess a $Pm\bar{3}m$ cubic pore structure (Fig. S4c, d and S5†). The color of MOF powder changes from white to bright purple after epitaxial growth of ZIF-67 layers on ZIF-8 SPPs (Fig. S6†). The powder X-ray diffraction (XRD) patterns of ZIF-8 SPPs and ZIF-8@ZIF-67 SPPs exhibit characteristic peaks corresponding to ZIF-8 and ZIF-67, respectively, further indicating the successful formation of ZIF-8@ZIF-67 (Fig. S7†). As shown in Fig. S8,† SEM and TEM images reveal that ZIF-8@ZIF-67 SPPs possess the same pore structure as ZIF-8 SPPs with a slightly reduced pore size. A high-magnification SEM image reveals that the thickness of the pore wall of ZIF-8@ZIF-67 SPPs after epitaxial growth increases from ~33 nm to ~43 nm, indicating that a thin ZIF-67 layer of 5 nm uniformly coats the surface of ZIF-8 SPPs. The SAXS pattern of ZIF-8@ZIF-67 SPPs exhibits a characteristic peak in a similar position to that of ZIF-8 SPPs, corresponding to the (100) reflection of an SP topology (Fig. S9†). High-angle annular dark-field scanning transmission electron microscopy (HAADF-STEM) images and corresponding energy-dispersive X-ray spectroscopy (EDX) elemental mappings further confirm the successful growth of ZIF-67 on ZIF-8 SPPs (Fig. S10†). The N_2 adsorption isotherms of ZIF-8 SPPs and ZIF-8@ZIF-67 SPPs exhibit a combination of type I and type IV characteristics, confirming their hierarchically porous structure (Fig. S11a and Table S1†). The Barrett–Joyner–Halenda (BJH) model is used to analyze the pore size distributions of ZIF-8 SPPs and ZIF-8@ZIF-67 SPPs, which indicates a decrease in pore size after epitaxial growth, further demonstrating the successful growth of an outer layer of ZIF-67 on ZIF-8 SPPs (Fig. S11b†).

After the thermal treatment under a N_2 atmosphere, Co/NC UDPPs retain the original 3D periodic channels present in the ZIF-8@ZIF-67 SPP precursors (Fig. 2a, b and S12†). Due to the shrinkage of the MOFs during thermal decomposition, the distance between the neighboring pores in Co/NC UDPPs becomes smaller than that of ZIF-8@ZIF-67 SPPs, although the pore size remains nearly completely unchanged (Fig. 2c). Further revealed by TEM at higher magnification, Co/NC UDPPs form a completely new 3D interconnected network of SP structural mesopores within the originally solid pore walls (Fig. 2d). The formation of the new mesopores is controlled by a heterogeneous interface-stabilized shrinkage process, which results from the differential thermal stability between the ZIF-8 network and ZIF-67 shell (Fig. S13†). During the thermal treatment, ZIF-67 decomposes first into a rigid Co/NC shell, which to some extent suppresses the inward contraction of the carbon framework. Simultaneously, Co provides the driving force for the outward expansion of the decomposing ZIF-8 into carbon, leading to the formation of a new set of mesopores inside the solid pore wall. We refer to these as internal pores, as they are distinct from the original pores inherited from the MOF precursors, which are open to the external environment. These internal pores, along with the originally existing ones, present a spatially unbalanced bicontinuous structure resembling $Im\bar{3}m$ (Fig. S14†). Some cracks can be observed on the newly formed thinner pore wall, which is decorated with Co nanoparticles that separate the two sets of pore channels (Fig. 2e and f). Locally, the pore structure of Co/NC UDPPs resembles interconnected nanotubes, with tube wall thicknesses of around 4.6 nm, which corresponds to the thickness of the ZIF-67 layer in their MOF precursors (Fig. S15†). High-resolution TEM (HRTEM) reveals a lattice spacing of 0.36 nm for the graphitic carbon in the pore

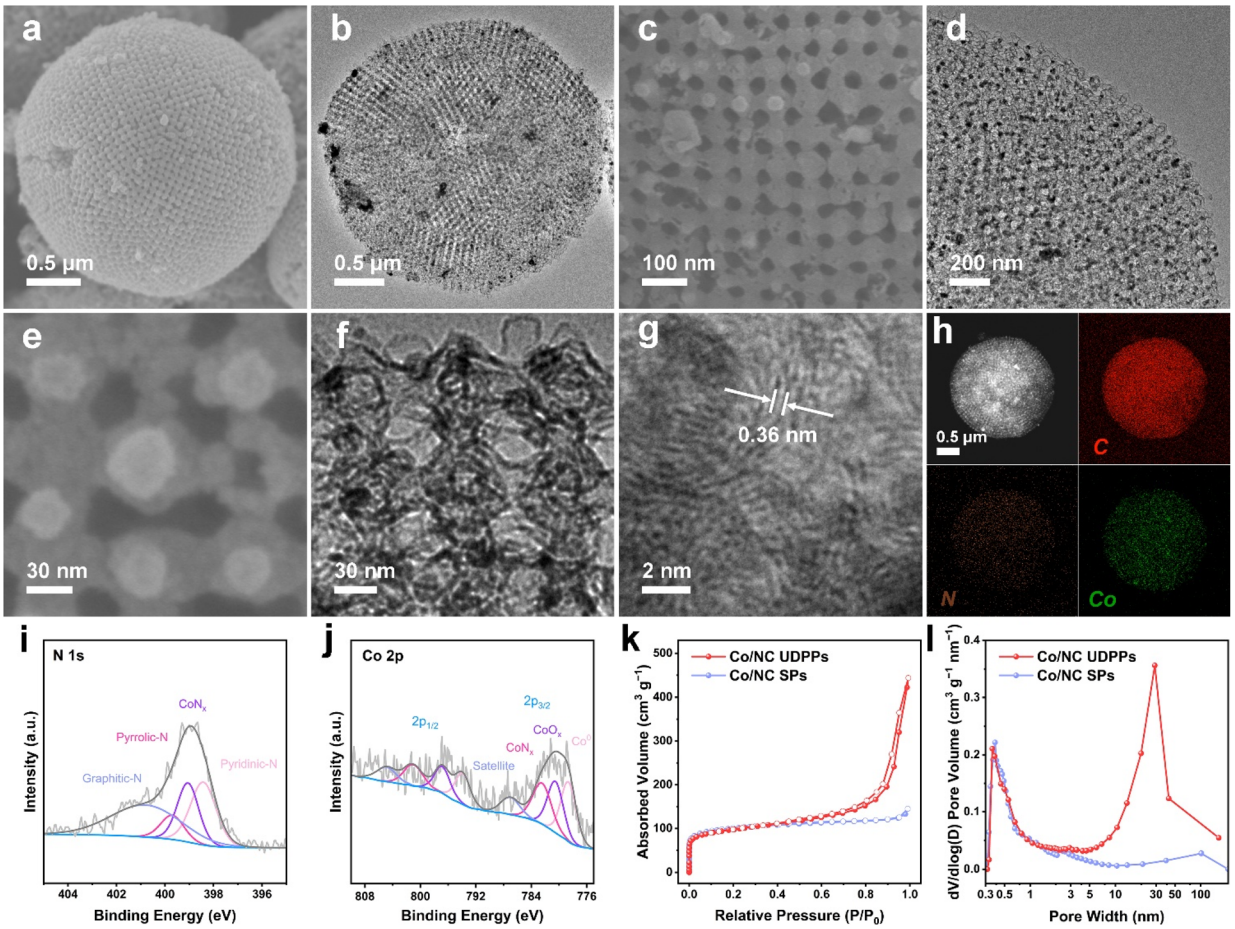

Fig. 2 Synthesis and characterization of the Co/NC UDPPs. (a, c and e) SEM and (b, d and f) TEM images of Co/NC UDPPs. (g) HRTEM image of a Co/NC UDPP. (h) HAADF-STEM and EDX elemental mapping images of a Co/NC UDPP. High-resolution (i) N 1s and (j) Co 2p XPS spectra of Co/NC UDPPs. (k) N_2 sorption isotherms and (l) NLDFT pore size distributions of Co/NC UDPPs and Co/NC SPs.

wall (Fig. 2g). The HAADF-STEM images and corresponding EDX elemental mappings demonstrate the uniform distribution of Co within the N-doped carbon framework (Fig. 2h).

The XRD pattern of Co/NC UDPPs exhibits two diffraction peaks around 44.4° and 51.6°, corresponding to the (111) and (200) planes of face-centered cubic metallic Co, respectively (Fig. S16a†). This indicates the formation of zero-valent Co during the pyrolysis process of the MOF. The Raman spectrum of Co/NC UDPPs exhibits a distinct D band and G band, corresponding to defective carbon and graphitic carbon, respectively (Fig. S16b†). The electronic structure and composition of the sample were investigated using X-ray photoelectron spectroscopy (XPS). The survey spectrum indicates the coexistence of C, N, Co, O, and residual Zn in Co/NC UDPPs (Fig. S16c†). Deconvolution of the high-resolution C 1s peak (Fig. S16d†) exhibits the presence of C–C/C=C (284.7 eV), C–O/C–N (285.2 eV), and C=O/C=N (286.4 eV). The N 1s spectrum (Fig. 2i) can be deconvoluted into four peaks, including pyridinic-N (398.4 eV), Co-coordinated N (399.1 eV), pyrrolic-N (399.7 eV), and graphitic-N (400.8 eV). The XPS spectrum of Co 2p for Co/NC UDPPs exhibits three peaks at 778.5 eV, 780.4 eV, and 782.3 eV, corresponding to Co, Co–O_x, and Co–N_x, respectively (Fig. 2j). It is worth noting that the strong coordination between Co and N is considered the primary active site in the ORR.[32] Distinct from the Co/N-doped carbon solid particles (designated as Co/NC SPs, Fig. S17†) derived from conventional microporous ZIF-67 crystals (Fig. S18†), the N_2 adsorption–desorption isotherms of Co/NC UDPPs exhibit a more obvious hysteresis loop, indicating that in addition to the micropores caused by the collapse of the MOF matrix during pyrolysis, there are also abundant meso-/macropores contributed by the bicontinuous structure (Fig. 2k). The Brunauer–Emmett–Teller (BET) surface areas of Co/NC UDPPs and Co/NC SPs are calculated to be 355 $m^2\ g^{-1}$ and 376 $m^2\ g^{-1}$, respectively (Table S1†). The total pore volume of Co/NC UDPPs is measured to be 0.67 $cm^3\ g^{-1}$, which is significantly higher than that of Co/NC SPs (0.22 $cm^3\ g^{-1}$, Table S1†). Additionally, the pore size distribution of Co/NC UDPPs calculated by using nonlocal density functional theory (NLDFT) reveals a wide range of meso-/macroporous distributions, which may be due to the coexistence of small mesopores or cracks in the pore wall, and two sets of channels with different volumes (Fig. 2l and S19†).

We utilized TEM to further investigate the spatial relative position and volume of the two sets of pores in Co/NC UDPP.

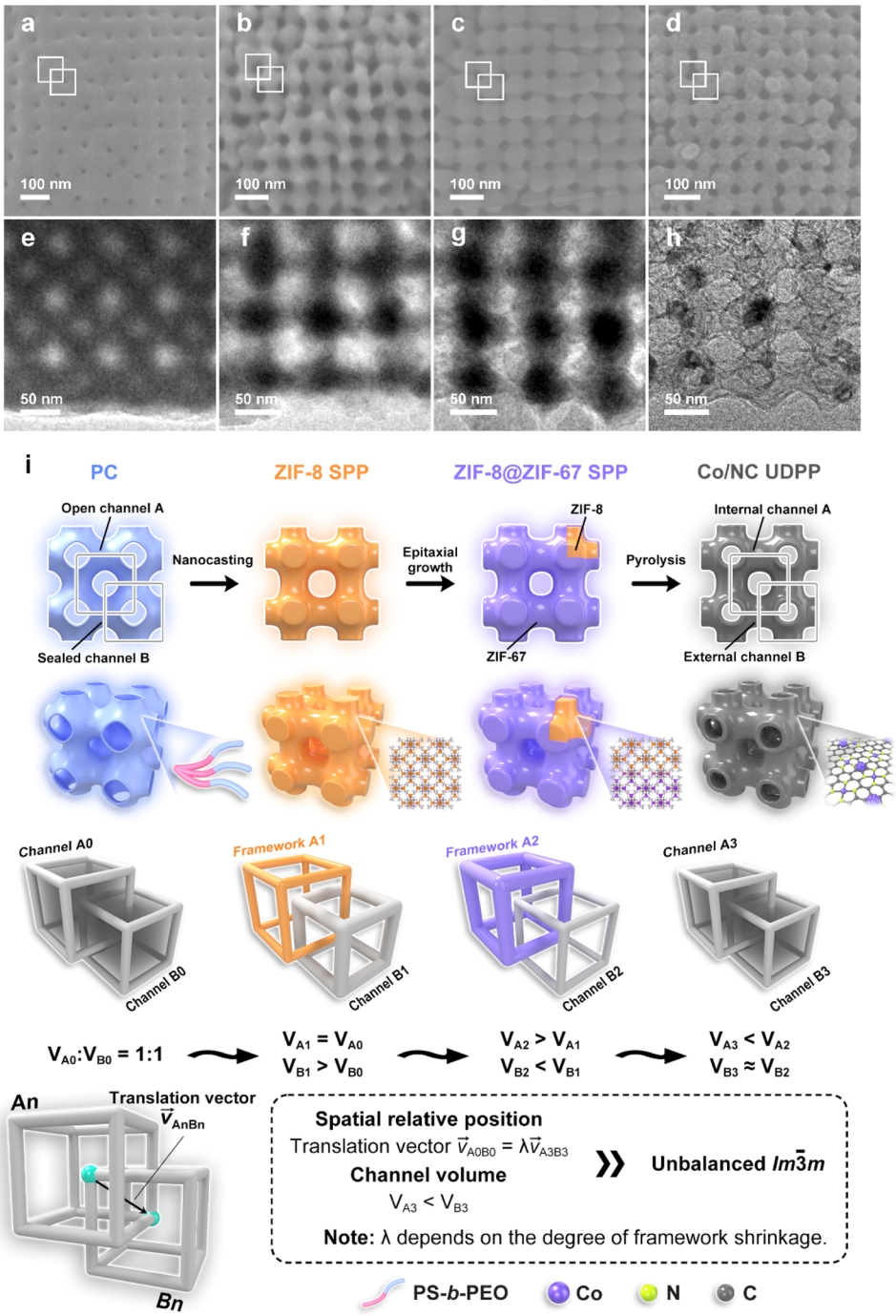

Fig. 3 Formation processes of Co/NC UDPP. (a–d) SEM and (e–h) TEM images of (a and e) PC, (b and f) ZIF-8 SPP, (c and g) ZIF-8@ZIF-67 SPP and (d and h) Co/NC UDPP along the [100] direction. (i) Schematic illustration of pore structure changes at different reaction stages. The spatial relative positions of A and B in panels (a–d) are represented by interlaced white boxes.

Fig. 3 presents the SEM and TEM images of intermediate products in the [100] direction during different reaction stages along with corresponding models. Within the PC, a distinctive DP topology is observed, comprising two sets of identical SP structural channels. To better comprehend the formation process of the unbalanced DP channels in the product, we designate the channels connected with the external environment within the PC as A0 and the internal sealed channels as B0. In the initial stage, the volume of the two sets of channels is the same ($V_{A0} = V_{B0}$). During the crystallization process of ZIF-8, the raw materials undergo diffusion and growth within the open channels marked as A0 in the bicontinuous template. This results in the formation of an overall framework with the same characteristics as the A0 channels. At this point, the spatial orientation of the channels in ZIF-8 SPP aligns with the B0 channels within the PC, while the channel volume V_{B1} becomes

larger compared to that in PC (V_{B0}) due to the removal of the polymer template. Following the epitaxial growth of ZIF-67 on ZIF-8 SPP, the pore wall of ZIF-8@ZIF-67 SPP becomes thicker, while the pore structure remains unchanged, which results in the increase of framework volume V_{A2} and decrease of channel volume V_{B2}. During the thermal treatment, a set of smaller-volume SP cubic structural channels forms within the initially solid framework, aligning spatially with channel A0. The shrinkage of the MOF skeleton reduces the volume of the internal channel V_{A3} while keeping the volume of the external channel V_{B3} nearly completely unchanged. At this stage, the two sets of Co/NC UDPP channels formed exhibit a similar spatial relative position to that of the initial channels within the PC, but with different pore volumes (Fig. S20†). This results in an unbalanced bicontinuous structure similar to $Im\bar{3}m$.

Considering its overall 3D open bicontinuous pore structure and local cracked thin-wall nanotube structure, Co/NC UDPP is expected to exhibit higher mass transfer efficiency and catalytically active surface utilization in the ORR. To verify the effects of structure on the electrochemical properties of the materials, we used Co/NC SPs and Co/N-doped carbon single primitive structural particles (designated as Co/NC SPPs, Fig. S21†) synthesized by pyrolysis of ZIF-67 single primitive structural particles (designated as ZIF-67 SPPs, Fig. S22, S23, and Table S1†) as control samples. The N_2 adsorption–desorption isotherms and corresponding pore size distribution reveal the hierarchically porous structure of Co/NC SPPs (Fig. S24 and Table S1†). Compared with Co/NC SPs, the single-network structure of Co/NC SPPs provides a set of continuous channels that significantly increase mass transfer and improve the utilization of active sites, and Co/NC UDPPs can further enhance the surface-to-volume ratio and provide more efficient mass diffusion through the unbalanced bicontinuous structure. The XRD patterns, Raman spectra, and XPS measurements of Co/NC SPs and Co/NC SPPs indicate their compositions and electronic structures are similar to those of Co/NC UDPPs (Fig. S25–S27†). The ORR performance of Co/NC UDPPs is evaluated using linear sweep voltammetry (LSV) in 0.1 M KOH at 1600 rpm. Among the samples synthesized at different carbonization temperatures, the Co/NC UDPPs synthesized by calcination at 700 °C exhibit the highest ORR activity (Fig. S28 and S29†). Compared to Co/NC SPs ($E_{1/2} = 0.829$ V, $J_L = 3.3$ mA cm^{-2}), Co/NC SPPs ($E_{1/2} = 0.842$ V, $J_L = 4.2$ mA cm^{-2}), and Pt/C ($E_{1/2} = 0.834$ V, $J_L = 4.7$ mA cm^{-2}), Co/NC UDPPs exhibit a higher half-wave potential and limiting current density ($E_{1/2} = 0.856$ V, $J_L = 4.7$ mA cm^{-2}), which surpass those of most Co/NC catalysts (Fig. 4a and Table S2†). Three Co/NC catalysts with different structures present Tafel slopes for the ORR in the order of Co/NC UDPPs < Co/NC SPPs < Co/NC SPs, indicating faster kinetics of the 3D interconnected pore structure (Fig. 4b). The electron transfer number (n) calculated by the rotating ring disk electrode test is close to 3.8, and the peroxide yield of Co/NC UDPPs is lower than that of Co/NC SPs and Co/NC SPPs, indicating that the reaction pathway from O_2 to OH^- involved a four-electron transfer (Fig. 4c). Meanwhile, the average value of n calculated from the Koutecký–Levich (K–L) plot is about 4.0 (Fig. S30†), which is consistent with the rotating ring disk electrode (RRDE) test results. The durability of Co/NC UDPPs is assessed using the constant potential chronoamperometry technique. After 30 000 s, the current density of Co/NC UDPPs remains at 86.0% of the initial ORR current at a potential of 0.7 V *versus* the reversible hydrogen electrode (*vs.* RHE), demonstrating significantly higher stability compared to Pt/C (69.4%, Fig. S31†). After the reaction, there are no significant changes observed in the structure and composition of Co/NC UDPPs (Fig. S32†). In addition, Co/NC UDPPs exhibit higher tolerance to methanol compared to Pt/C, as there is no significant change in the current density after methanol addition (Fig. S33†).

To highlight the superiority of the Co/NC UDPPs, the finite element method is used to simulate the localized reaction environments. Based on the TEM images of samples, the 3 × 3 × 3 structural units of the materials with different pore structures are used as models for simulations (Fig. 4d–f). In addition, a constant ORR rate is added to the models while keeping the flow rate constant. The cross sections through the center of the models along the liquid flow direction are selected for the analysis of the results. As shown in Fig. 4g–i and S34,† the O_2 concentration in the model of Co/NC UDPP is significantly higher than that in Co/NC SP and Co/NC SPP. For Co/NC SP without continuous channels, the O_2 concentration in the model presents a low level due to the low diffusion rate of the electrolyte in the narrow micro/mesopores, which reduces the utilization rate of the active site inside the material. For Co/NC SPP with one set of continuous channels, the O_2 concentration in the solid pore wall remains low, whereas the O_2 concentration in the channels is significantly increased. This can be attributed to that O_2 could enter the model through the rapid flow of electrolyte in the continuous channel, and the O_2 content per unit time through the model increases significantly. Among the three models, Co/NC UDPP with two sets of pore structures exhibits the highest O_2 concentration, which can be attributed to efficient mass transfer resulting from two sets of 3D open channels. Moreover, the thin pore walls facilitate the penetration of the electrolyte into the interior of Co/NC UDPP, increasing the accessibility of the active sites. To intuitively demonstrate the advantages of the bicontinuous structure, a straight line is taken along the direction of liquid flow through the continuous channel of the Co/NC SPP, with equivalent lines drawn at the same positions in the other two models for comparison. The O_2 concentrations and OH^- concentrations corresponding to each point on the lines are depicted using line graphs (Fig. 4j–l and S35†). The overall O_2 concentrations in the three models show a gradient decline, which is due to the gradual consumption of O_2 by the ORR. Compared with the sharp decrease of O_2 concentration in Co/NC SP, the decline trend of O_2 concentration in Co/NC SPP and Co/NC UDPP is moderate. Three models with different pore structures present O_2 concentration in the order of Co/NC UDPP > Co/NC SPP > Co/NC SP, which further indicates the advantage of open channels. It is worth noting that the sudden increase in O_2 concentration at the rear of Co/NC SP is attributed to the gradual diffusion of the electrolyte from the back of the model to its interior. Moreover, within the framework material, the low mass transfer

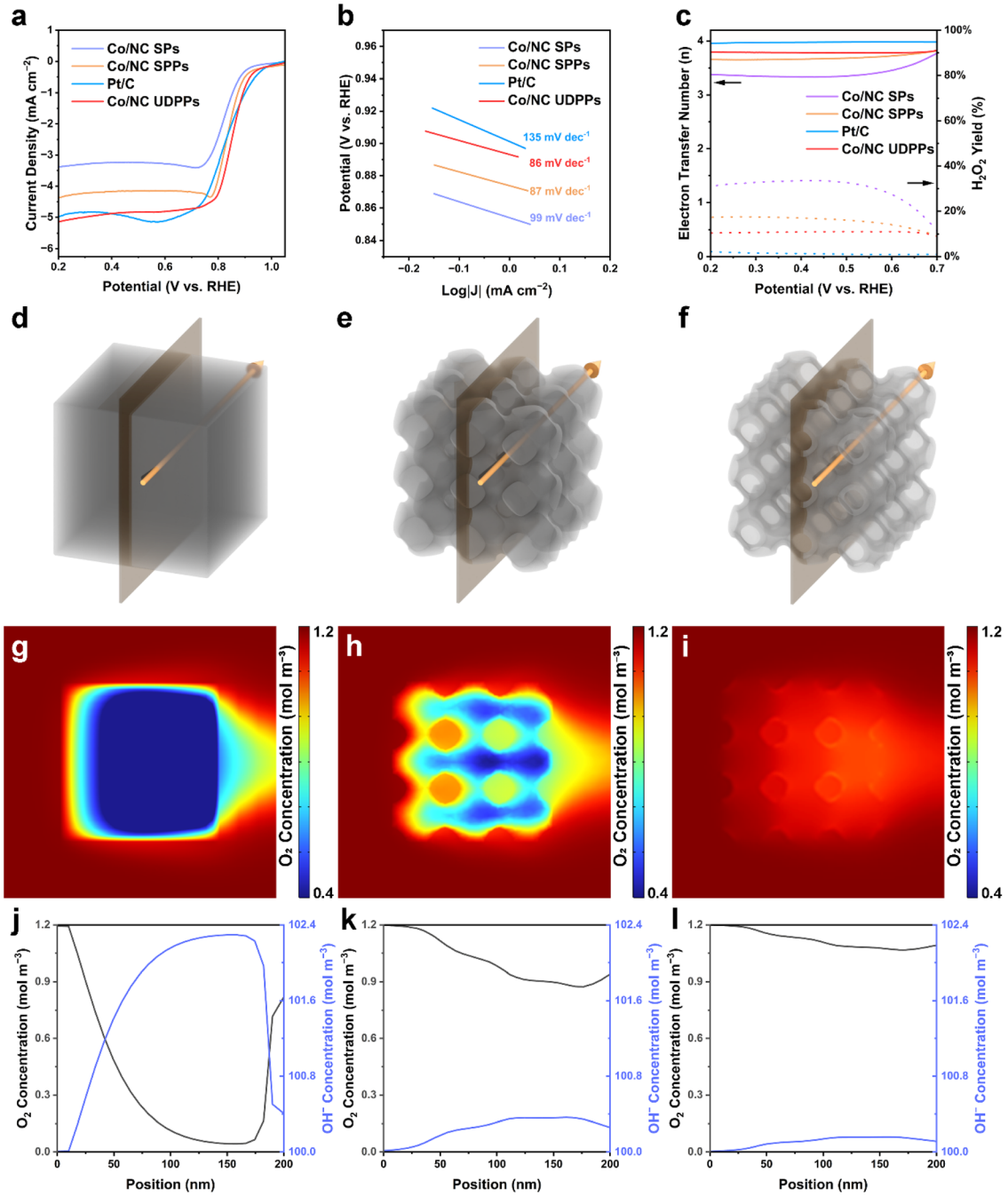

Fig. 4 ORR catalytic performances of all samples and their finite element simulations. (a) LSV curves, (b) Tafel curves, and (c) electron-transfer number and H_2O_2 yield of Co/NC SPs, Co/NC HPs, Co/NC UDPPs, and Pt/C. (d–f) Schematic illustrations of simulation models and selected locations for (d) Co/NC SP, (e) Co/NC SPP, and (f) Co/NC UDPP. (g–i) Cross sections illustrating O_2 concentration distributions for (g) Co/NC SP, (h) Co/NC SPP, and (i) Co/NC UDPP. (j–l) The distributions of O_2 concentrations and OH^- concentrations along the arrow directions for (j) Co/NC SP, (k) Co/NC SPP, and (l) Co/NC UDPP.

rate causes the accumulation of *in situ* generated OH^- ions, leading to an opposite trend in OH^- concentration compared to O_2 concentration (Fig. S36†), thereby inhibiting the reaction process associated with the $4e^-$ pathway of the electrocatalyst.[33,34] The experiments and simulations reveal that the 3D open channels of the bicontinuous structure could provide a more efficient diffusion path, enhance O_2 adsorption and oxide removal, and alleviate the sluggish kinetics of the ORR. The local nanotube structure and the cracks on the tube wall connect the two sets of pore structures, which is conducive to the utilization of the inner tube wall and improves the overall surface utilization of the structure (Fig. S37†).

To explore the practical application of Co/NC UDPPs, an aqueous ZAB is assembled with Co/NC UDPPs as the air cathode

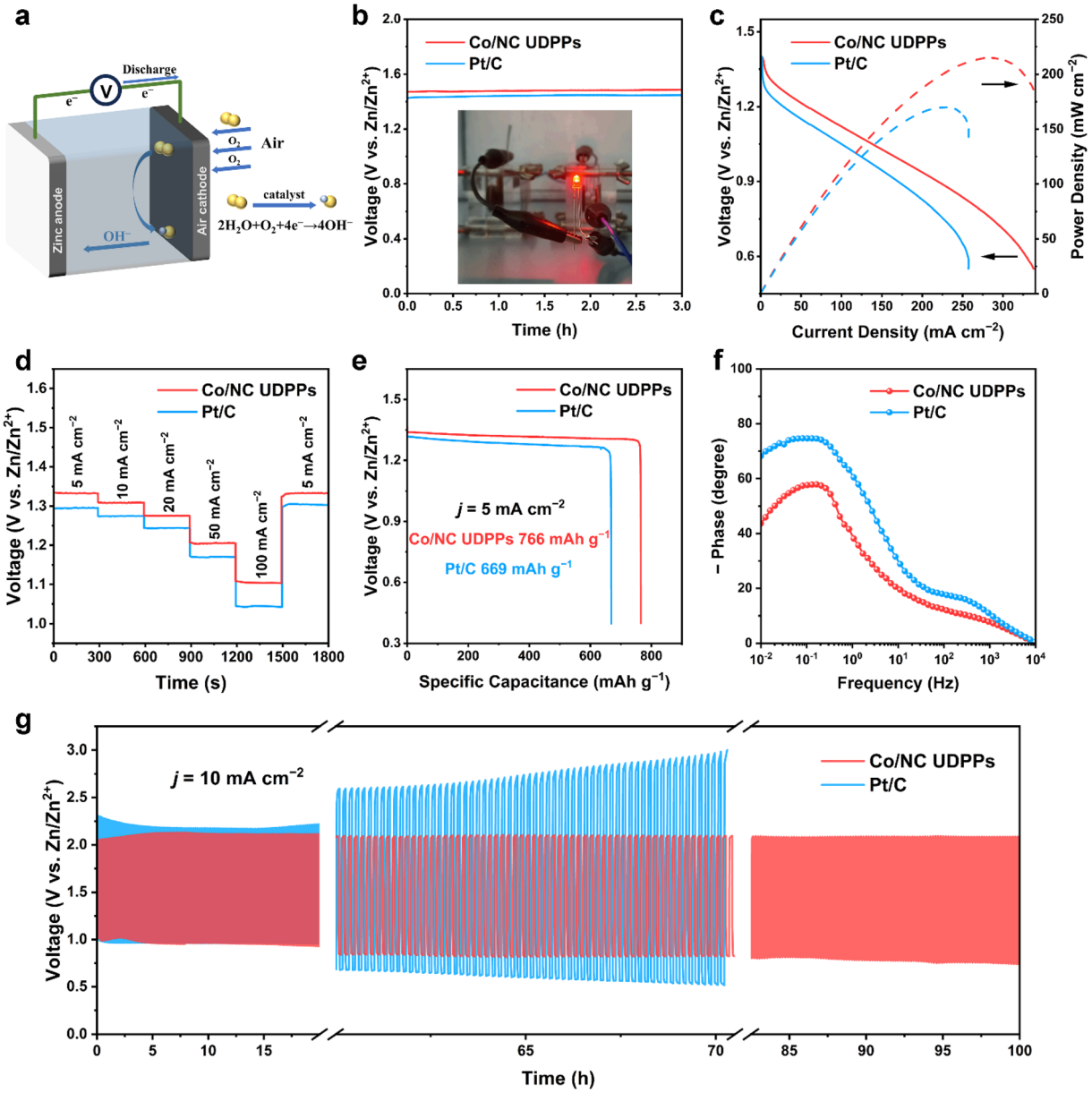

Fig. 5 Battery performance of ZABs with Co/NC UDPPs or Pt/C as the air cathode catalyst. (a) Schematic. (b) Open circuit voltage curves (inset: a photograph of two batteries connected in series lighting a LED). (c) Polarization and power density curves. (d) Rate performances at varied current densities. (e) Galvanostatic discharge profiles at 10 mA cm^{-2}. (f) Bode phase angle plots. (g) Long-term charge–discharge cycling curves at 10 mA cm^{-2}.

(Fig. 5a). As shown in Fig. 5b, the Co/NC UDPP-based ZAB exhibits a higher open circuit voltage of 1.48 V, compared to 1.44 V for the Pt/C-based ZAB, bringing it closer to the theoretical value of 1.64 V. The inset shows that two Co/NC UDPP-based ZABs connected in series can power an LED light. Moreover, the power density of the ZAB based on Co/NC UDPPs is measured to be 215 mW cm^{-2}, far exceeding that of the Pt/C-based battery (170 mW cm^{-2}) and those of ZABs assembled with other Co-based catalysts reported previously (Fig. 5c and Table S3†). The measurement of the rate performance also demonstrates a superior discharge ability of the Co/NC UDPP-based ZAB, in which the discharge voltage remains at a high level of 1.1 V even at a current density of 100 mA cm^{-2} (Fig. 5d). Additionally, the specific capacity of the Co/NC UDPP-based ZAB is determined to be 766 mA h g^{-1}, which is higher than that of the Pt/C-based ZAB (669 mA h g^{-1}, Fig. 5e). The electrochemical impedance spectra (EIS) indicate that the ohmic resistance (R_s) and charge transfer resistance (R_{ct}) of the Co/NC UDPP-based ZAB are both smaller than those of the Pt/C-based ZAB, indicating that Co/NC UDPPs can accelerate the mass transfer kinetics (Fig. S38 and Table S4†). The phase angle values determined from the Bode phase angle plot can intuitively show the difficulty of charge transfer across the interface of the materials. In general, the larger phase angle value indicates a harder charge transfer.[35] As shown in Fig. 5f, the Bode phase angle value of the Co/NC UDPPs is much smaller than

that of the Pt/C, indicating that the Co/NC UDPP electrode exhibits a better active interface in the electrocatalytic processes, which is due to the high-efficiency mass transfer enabled by the 3D open channels of the bicontinuous structure and high surface utilization enabled by the local thin nanotube structure. The long-term durability measurement is carried out by galvanostatic charge–discharge cycling at the current density of 10 mA cm^{-2} (Fig. 5g), and the ZAB based on Co/NC UDPPs stably cycles for more than 100 h. In contrast, the charge and discharge voltage gap of the Pt/C-based ZAB exhibits a substantial voltage shift due to the gradual intensification of polarization. Co/NC UDPPs have proved to be an excellent ORR catalyst for rechargeable ZABs due to their unique pore structure, which is conducive to rapid mass transfer and improves the utilization efficiency of the catalyst.

Conclusions

In summary, a heterogeneous interface-induced topological phase transition method has been demonstrated to achieve precise synthesis of unbalanced double primitive bicontinuous architectural Co/NC. In this method, the single primitive structural ZIF-8 is constructed with bicontinuous polymer cubosomes as the template, and then ZIF-67 is epitaxially grown on ZIF-8. Based on the differences in thermal stability at the heterogeneous interface of ZIF-8 and ZIF-67 during pyrolysis, a new set of single primitive channels is constructed in the solid pore wall while maintaining the original pore structure. The spatial relative position of the two sets of channels is the same as that of the polymer template, but the pore volume is different, resulting in an unbalanced bicontinuous structure similar to that of $Im\bar{3}m$. Benefiting from the high-efficiency mass transfer enabled by the 3D open pore structure and the high surface utilization enabled by the local thin-wall nanotube structure, the as-prepared Co/NC UDPPs exhibit enhanced electrochemical performance in the ORR. Moreover, the ZAB using Co/NC UDPPs as the air cathode electrocatalyst exhibits higher peak power density, larger specific capacity, and better cycling stability than those assembled with commercial Pt/C. This heterogeneous interface-induced topological phase transition method opens up new opportunities for the fine construction of extra channels to achieve 3D periodic interpenetrating networks through rational design and processing of porous heterostructures. Such special networks are expected to exhibit extraordinary performances in catalysis, energy conversion, and cargo delivery.

Data availability

All the data supporting this article have been included in the main text and the ESI.†

Author contributions

B. G. conceived the project. B. Z. prepared the materials, performed the measurements and analysed the data. B. L., J. H., R. S., H. X., Y. S., G. C., Z. S., C. L., Y. G., and M. Z. helped with some of the experiments and characterization. All authors discussed the results and commented on the manuscript. B. Z. wrote the draft, while S. L. Z., Y. Y., and B. G. revised and finalized the manuscript.

Conflicts of interest

There are no conflicts to declare.

Acknowledgements

We thank the National Natural Science Foundation of China (Grant 22375071, 22288101, and 21920102005), the National Key Research and Development Program of China (Grant 2021YFA1501202 and 2022YFA1503600), and the "111 Center" (B17020) for supporting this work.

Notes and references

1 X. Xie, C. He, B. Li, Y. He, D. A. Cullen, E. C. Wegener, A. J. Kropf, U. Martinez, Y. Cheng, M. H. Engelhard, M. E. Bowden, M. Song, T. Lemmon, X. S. Li, Z. Nie, J. Liu, D. J. Myers, P. Zelenay, G. Wang, G. Wu, V. Ramani and Y. Shao, *Nat. Catal.*, 2020, **3**, 1044–1054.
2 E. Jung, H. Shin, B.-H. Lee, V. Efremov, S. Lee, H. S. Lee, J. Kim, W. Hooch Antink, S. Park, K.-S. Lee, S.-P. Cho, J. S. Yoo, Y.-E. Sung and T. Hyeon, *Nat. Mater.*, 2020, **19**, 436–442.
3 J. Li, M. T. Sougrati, A. Zitolo, J. M. Ablett, I. C. Oğuz, T. Mineva, I. Matanovic, P. Atanassov, Y. Huang, I. Zenyuk, A. Di Cicco, K. Kumar, L. Dubau, F. Maillard, G. Dražić and F. Jaouen, *Nat. Catal.*, 2021, **4**, 10–19.
4 M. Lefèvre, E. Proietti, F. Jaouen and J.-P. Dodelet, *Science*, 2009, **324**, 71–74.
5 J. P. Collman, L. Fu, P. C. Herrmann and X. Zhang, *Science*, 1997, **275**, 949–951.
6 E. Luo, Y. Chu, J. Liu, Z. Shi, S. Zhu, L. Gong, J. Ge, C. H. Choi, C. Liu and W. Xing, *Energy Environ. Sci.*, 2021, **14**, 2158–2185.
7 B. Tang, Y. Zhou, Q. Ji, Z. Zhuang, L. Zhang, C. Wang, H. Hu, H. Wang, B. Mei, F. Song, S. Yang, B. M. Weckhuysen, H. Tan, D. Wang and W. Yan, *Nat. Synth.*, 2024, **3**, 878–890.
8 W. Yao, A. Hu, J. Ding, N. Wang, Z. Qin, X. Yang, K. Shen, L. Chen and Y. Li, *Adv. Mater.*, 2023, **35**, 2301894.
9 X. Tang, Y. Wei, W. Zhai, Y. Wu, T. Hu, K. Yuan and Y. Chen, *Adv. Mater.*, 2023, **35**, 2208942.
10 B. Y. Guan, X. Y. Yu, H. B. Wu and X. W. Lou, *Adv. Mater.*, 2017, **29**, 1703614.
11 B. Zhao, J. Han, B. Liu, S. L. Zhang and B. Guan, *Chem. Synth.*, 2024, **4**, 41.
12 G. Cai, P. Yan, L. Zhang, H.-C. Zhou and H.-L. Jiang, *Chem. Rev.*, 2021, **121**, 12278–12326.
13 J. Han, H. Xu, B. Zhao, R. Sun, G. Chen, T. Wu, G. Zhong, Y. Gao, S. L. Zhang, Y. Yamauchi and B. Guan, *J. Am. Chem. Soc.*, 2024, **146**, 18979–18988.
14 H. Xu, J. Han, B. Zhao, R. Sun, G. Zhong, G. Chen, Y. Yamauchi and B. Guan, *Nat. Commun.*, 2023, **14**, 8062.

15 T. Wu, G. Chen, J. Han, R. Sun, B. Zhao, G. Zhong, Y. Yamauchi and B. Guan, *J. Am. Chem. Soc.*, 2023, **145**, 16498–16507.
16 G. Zhong, G. Chen, J. Han, R. Sun, B. Zhao, H. Xu, S. Wang, Y. Yamauchi and B. Guan, *ACS Nano*, 2023, **17**, 25061–25069.
17 L. Han and S. Che, *Adv. Mater.*, 2018, **30**, 1705708.
18 L. Xiang, Q. Li, C. Li, Q. Yang, F. Xu and Y. Mai, *Adv. Mater.*, 2023, **35**, 2207684.
19 K. Hur, Y. Francescato, V. Giannini, S. A. Maier, R. G. Hennig and U. Wiesner, *Angew. Chem., Int. Ed.*, 2011, **50**, 11985–11989.
20 J. Llandro, D. M. Love, A. Kovács, J. Caron, K. N. Vyas, A. Kákay, R. Salikhov, K. Lenz, J. Fassbender, M. R. J. Scherer, C. Cimorra, U. Steiner, C. H. W. Barnes, R. E. Dunin-Borkowski, S. Fukami and H. Ohno, *Nano Lett.*, 2020, **20**, 3642–3650.
21 Z. Lin, J. Zhou, C. Cortez-Jugo, Y. Han, Y. Ma, S. Pan, E. Hanssen, J. J. Richardson and F. Caruso, *J. Am. Chem. Soc.*, 2020, **142**, 335–341.
22 C. Tang, W. Lu, Y. Zhang, W. Zhang, C. Cui, P. Liu, L. Han, X. Qian, L. Chen, F. Xu and Y. Mai, *Adv. Mater.*, 2024, **36**, 2402005.
23 W. Mao, X. Cao, Q. Sheng, L. Han and S. Che, *Angew. Chem., Int. Ed.*, 2017, **56**, 10670–10675.
24 L. Han, D. Xu, Y. Liu, T. Ohsuna, Y. Yao, C. Jiang, Y. Mai, Y. Cao, Y. Duan and S. Che, *Chem. Mater.*, 2014, **26**, 7020–7028.
25 H.-Y. Hsueh, Y.-C. Ling, H.-F. Wang, L.-Y. C. Chien, Y.-C. Hung, E. L. Thomas and R.-M. Ho, *Adv. Mater.*, 2014, **26**, 3225–3229.
26 Y. Liu, Q. Zhou, H. Yu, Q. Yang, M. Wang, C. Huang, L. Xiang, C. Li, T. Heine, G. Hu, S. Wang, X. Feng and Y. Mai, *Angew. Chem., Int. Ed.*, 2024, **63**, e202400985.
27 J. Kibsgaard, Z. Chen, B. N. Reinecke and T. F. Jaramillo, *Nat. Mater.*, 2012, **11**, 963–969.
28 C. Li, Y. Pan, T. Xiao, L. Xiang, Q. Li, F. Tian, I. Manners and Y. Mai, *Angew. Chem., Int. Ed.*, 2023, **62**, e202215985.
29 B. He, Q. Zhang, Z. Pan, L. Li, C. Li, Y. Ling, Z. Wang, M. Chen, Z. Wang, Y. Yao, Q. Li, L. Sun, J. Wang and L. Wei, *Chem. Rev.*, 2022, **122**, 10087–10125.
30 H. Zhang, M. Zhang, R. Liu, T. He, L. Xiang, X. Wu, Z. Piao, Y. Jia, C. Zhang, H. Li, F. Xu, G. Zhou and Y. Mai, *Nat. Commun.*, 2024, **15**, 5451.
31 Z. Lin, S. Liu, W. Mao, H. Tian, N. Wang, N. Zhang, F. Tian, L. Han, X. Feng and Y. Mai, *Angew. Chem., Int. Ed.*, 2017, **56**, 7135–7140.
32 W. Xu, R. Zeng, M. Rebarchik, A. Posada-Borbón, H. Li, C. J. Pollock, M. Mavrikakis and H. D. Abruña, *J. Am. Chem. Soc.*, 2024, **146**, 2593–2603.
33 C. Yang, F. Sun, Z. Qu, X. Li, W. Zhou and J. Gao, *ACS Energy Lett.*, 2022, **7**, 4398–4407.
34 L. Jing, W. Wang, Q. Tian, Y. Kong, X. Ye, H. Yang, Q. Hu and C. He, *Angew. Chem., Int. Ed.*, 2024, **63**, e202403023.
35 L. Yan, B. Xie, C. Yang, Y. Wang, J. Ning, Y. Zhong and Y. Hu, *Adv. Energy Mater.*, 2023, **13**, 2204245.